Title

Transport of Heat by Hydrothermal Circulation in a Young Rift Setting: Observations From the Auka and JaichMaa Ja'ag' Vent Field in the Pescadero Basin, Southern Gulf of California

Journal

Journal of Geophysical Research: Solid Earth, 126(8)

ISSN

2169-9313

Authors

Negrete-Aranda, Raquel
Neumann, Florian
Contreras, Juan
et al.

Publication Date

2021-08-01

DOI

10.1029/2021jb022300

Peer reviewed

JGR Solid Earth

RESEARCH ARTICLE
10.1029/2021JB022300

Key Points:

- The Pescadero Basin is an incipient oceanic rift basin with vigorous hydrothermal activity along graben-bounding faults
- Aspects of the thermal regime of rifting of this basin are explored using an analytical model that incorporates conjugate heat transfer
- Hydrothermal circulation modeling shows an enormous exchange of heat takes place through fault walls to the surrounding sediments

Supporting Information:

Supporting Information may be found in the online version of this article.

Correspondence
R. Negrete-Aranda,
rnegrete@cicese.mx

Citation:
Negrete-Aranda, R., Neumann, F., Contreras, J., Harris, R. N., Spelz, R. M., Zierenberg, R., & Caress, D. W. (2021). Transport of heat by hydrothermal circulation in a young rift setting: Observations from the Auka and JaichMaa Ja'ag' vent field in the Pescadero Basin, southern Gulf of California. *Journal of Geophysical Research: Solid Earth*, *126*, e2021JB022300. https://doi.org/10.1029/2021JB022300

Received 28 APR 2021
Accepted 17 JUL 2021

Transport of Heat by Hydrothermal Circulation in a Young Rift Setting: Observations From the Auka and JaichMaa Ja'ag' Vent Field in the Pescadero Basin, Southern Gulf of California

Raquel Negrete-Aranda[1], Florian Neumann[2], Juan Contreras[2], Robert N. Harris[3], Ronald M. Spelz[4], Robert Zierenberg[5], and David W. Caress[6]

[1]Departamento de Geología, Catedrático CONACYT, Laboratorio de Tectonofísica y Flujo de Calor, CICESE, Ensenada, Mexico, [2]Departamento de Geología, Laboratorio de Tectonofísica y Flujo de Calor, CICESE, Ensenada, Mexico, [3]College of Earth, Ocean, and Atmospheric Sciences, Oregon State University, Corvallis, OR, USA, [4]Departamento de Geología, Facultad de Ciencias Marinas, Universidad Autónoma de Baja California, Campus Ensenada, Ensenada, Mexico, [5]Department of Earth and Planetary Sciences, University of California, Davis, CA, USA, [6]Monterey Bay Aquarium Research Institute, Moss Landing, CA, USA

Abstract Heat flow measurements collected throughout the Auka and JaichMaa Ja'ag' hydrothermal vent fields in the central graben of the Southern Pescadero Basin, southern Gulf of California, indicate upflow of hydrothermal fluids associated with rifting dissipate heat in excess of 10 W/m^2 around faults that have a few kilometers in length. Paradoxically, longer faults do not show signs of venting. Heat flow anomalies slowly decay to background values of ~2 W/m^2 at distances of ~1 km from these faults following an inverse square-root distance law. We develop a near-fault model of heat transport in steady state for the Auka vent field based on the fundamental Green's function solution of the heat equation. The model includes the effects of circulation in fracture networks, and the lateral seepage of geothermal brines to surrounding hemipelagic sediments. We use an optimal fitting method to estimate the reservoir depth, permeability, and circulation rate. Independently derived constraints for the model, indicate the heat source is at a depth of ~5.7 km; from the model, permeability and flow rates in the fracture system are $\sim 10^{-14}$ m^2 and 10^{-6} m/s, respectively, and $\sim 10^{-16}$ m^2 and 10^{-8} m/s in the basin aquitards, respectively. Model results point to the importance of fault scaling laws in controlling sediment-hosted vent fields and slow circulation throughout low permeability sediments in controlling the brine's chemistry. Although the fault model seems appropriate and straightforward for the Pescadero vents, it does seem to be the exception to the other known sediment-hosted vent fields in the Pacific.

Plain Language Summary The Earth cools down primarily by the release of heat transported from the planetary interior by magmas and hydrothermal fluids to the surface. A global system of underwater mountain ranges, ridge flanks, dissipate most of that heat while simultaneously forming new oceanic lithosphere. Porous pathways formed by fault networks and porous layers ultimately guide the process in the brittle upper crust. The Auka and JaichMaa Ja'ag' hydrothermal vent fields in the central graben of the Pescadero Basin, southern Gulf of California, are exemplary cases to study this process. We develop a model for heat transport that is, rather simple and straightforward that explains quite well the dissipation of heat observed across the Auka hydrothermal vent field and the chemistry of its waters. In our case, the motion of fluids by hydrothermal flow through porous layers causes a steady transference of heat across fault walls into its surroundings, forming a heat flow anomaly that decays as the square root of distance.

1. Introduction

Hydrothermal vent fields on the ridge flanks of oceanic basins are the loci of an enormous exchange of heat and solutes transported by fluids between the oceanic crust and overlying water masses (Lister, 1972; Sleep & Wolery, 1978; Wolery & Sleep, 1976). Moreover, seafloor hydrothermal circulation plays a critical role in our planet's thermal cooling and dynamic evolution. Considering that nearly 25% of the Earth's heat is lost by hydrothermal circulation through the oceanic crust (Lowell et al., 1995), it is evident that active venting

areas around mid-ocean ridges are crucial spots that control the long-term rate at which these processes occur.

Since their discovery in the mid '70s, hydrothermal vents have been studied in increasing detail using higher-resolution tools, bringing new clues about the factors controlling fluid migration in the lithosphere and seafloor discharge (Ondréas et al., 2018). While inferences regarding the subsurface plumbing of these systems have been made using local temperature measurements, geochemical data, and seismic surveys, few observations provide the necessary detail to resolve the components of the geothermal system feeding the vent fields. Here, we report a fine-scale heat flow survey in the southern Pescadero Basin, in the south-central Gulf of California (Figure 1A). Of the spreading systems in the Gulf of California (GC), the Pescadero basin represents a unique opportunity to study the basin's thermal regime in the early stages of rifting and hydrothermal venting. Extensive mapping of this basin by autonomous underwater vehicles (AUV's) at a resolution of ∼1 m in the horizontal plane and ∼1 cm in the vertical axis (Figure 1B; Paduan et al., 2018) revealed a series of active vents and diffuse flow clustered in two broad fields: The Auka hydrothermal field in the southern Pescadero Basin and the JaichMaa Ja'ag' vent, farther south (Figure 1B; Paduan et al., 2018). The hydrothermal activity was sampled and characterized by remote-operated underwater vehicles (ROV) during expeditions led by Monterey Bay Aquarium Research Institute (MBARI) and the Schmidt Ocean Institute (SOI) in 2015 and 2018. Analyses of waters and gases suggest that both vent fields share a common high-temperature hydrothermal reservoir in the permeable basaltic crust.

Because the heat flow data were collected systematically from an ROV at a sufficiently fine scale across the Auka vent field, the various processes influencing spatial variability in heat flow can be assessed, allowing us to constrain the depth of the hydrothermal reservoir beneath the vent field and intensity of convective heat transport both in the fractured rock system and porous sediments. To do so, we use a theoretical description of the transport of heat in porous media that combines the different elements of the Auka geothermal system. By assuming steady state and other pertinent approximations and simplifying assumptions we find analytical solutions that explain the heat flow measurements and predict scaling relationships consistent with the data and structural observations. The appeal of using analytical solutions is that it allows for the use of fast parameter identification algorithms, from which we characterize the convective state of the vent field. In contrast, the procedure remains cumbersome in more complex nonlinear dynamic numerical models due to nonconvexity, parameter sensitivity, and high computational cost.

We also report a handful of new heat flow measurements in the JaichMaa Ja'ag' that provide a broader vision of the thermal state of the Pescadero Basin. Furthermore, we investigate the energy exchange between fluids and host rock, something that has been overlooked so far, and how its physical properties, such as permeability, impact fluid flow dynamics. Sampling also permitted a comparison with heat flow patterns from sedimented sections of the Juan de Fuca Ridge, and examination of how a sediment cap affects the geometry of fluid flow and the modes of heat extraction in a young rifted setting.

2. The Gulf of California

Rifting in the Gulf began at ∼12–15 Ma when subduction ended west of the Baja California peninsula. As the East Pacific Rise approached the Pacific trench of North America, the subducting Farallón plate broke into several microplates, and, as subduction stalled, those microplates and the Baja California peninsula coupled to the Pacific plate, resulting in the modern divergent plate boundary observed within the Gulf of California (Lonsdale, 1995; Negrete-Aranda et al., 2013; Plattner et al., 2007). The peninsula moves nearly entirely with the Pacific plate. Translation and extension across the Gulf of California represent ∼92% of Pacific-North America relative motion (Persaud et al., 2017; Plattner et al., 2007).

Seafloor spreading began ca. 3.5 Ma ago, when the Baja Peninsula separated from the mainland of Mexico, and new oceanic crust emerged in the southern gulf (Lizarralde et al., 2007). Deformation in the Gulf of California (GC) is accommodated by a large variety of extension mechanisms that include high angle normal faults, gravitational spreading, crustal-scale stepovers, en-echelon extensional zones or sub-basins in areas of basaltic underplating, etc. (e.g., Bialas & Buck, 2009; Contreras-Pérez et al., 2012; Macias-Iñiguez

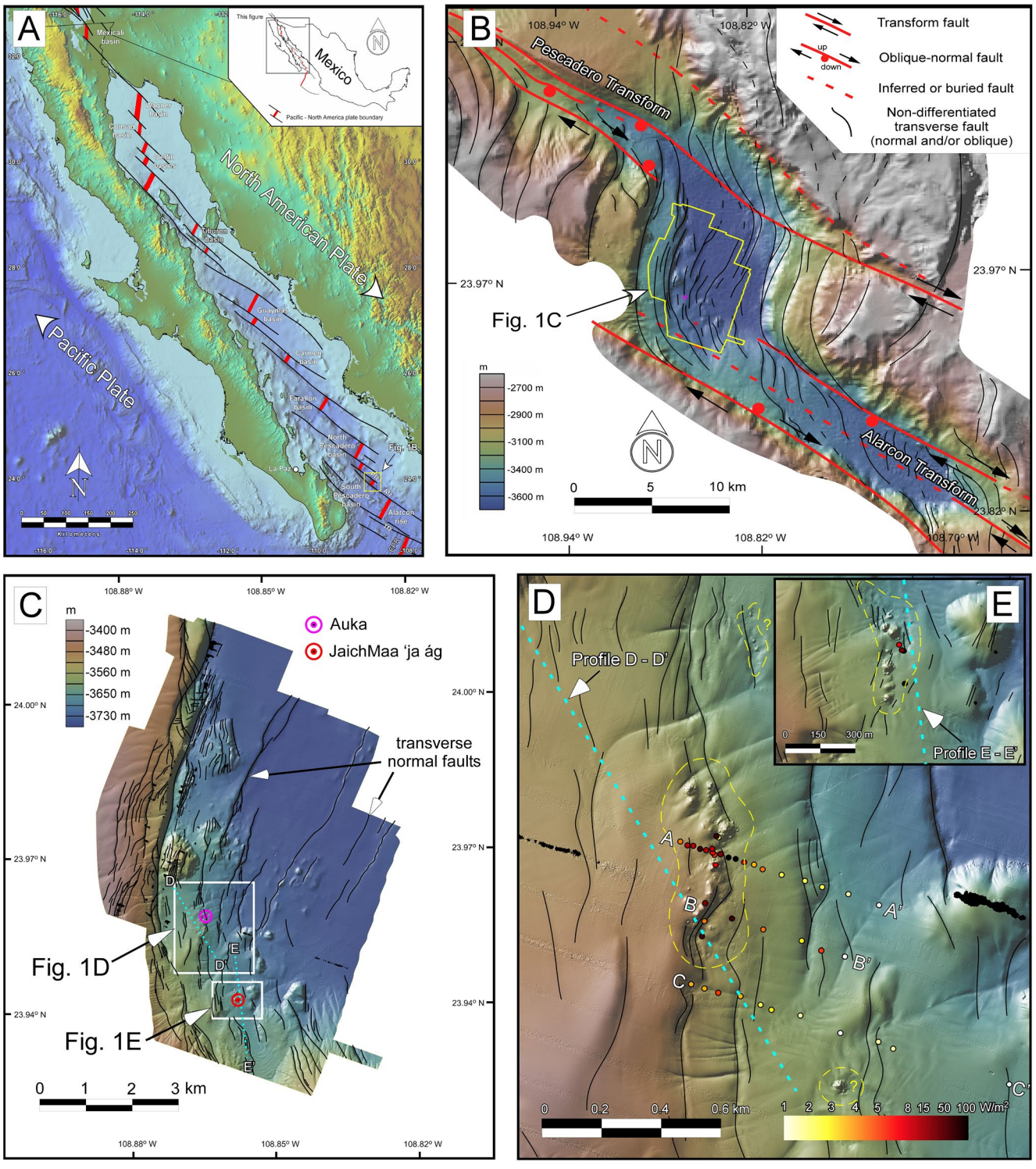

Figure 1.

et al., 2019; Martín-Barajas et al., 2013; Neumann et al., 2017; Persaud et al., 2017). Of the segments accommodating spreading, the 50 km Alarcón Rise is the longest and lies at the Gulf's mouth between the southern tip of the Peninsula and mainland Mexico (Figure 1A, Clague et al., 2018). Its full spreading rate is about 49 mm/yr (DeMets et al., 2010). At its southwestern end, the Alarcón Rise is bounded by the ~60 km-long Tamayo Transform Fault, whereas to the northeast, the plate boundary enters the GC and connects

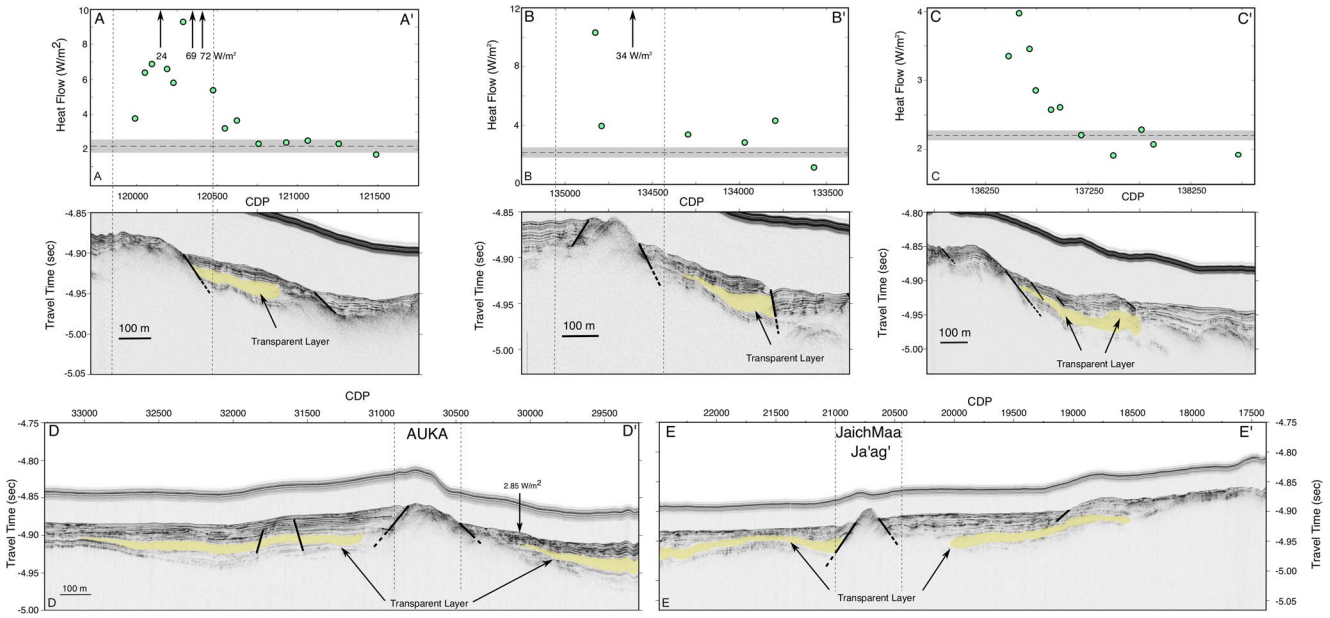

Figure 2. Heat flow measurements and simple interpreted sub-bottom profiles for (A) Northern A-A' (B) Central B-B' and (C) Southern C-C' transects. Heat flow data values are shown as green circles, whereas the average background heat flow value (2.2 ± 0.4 W/m^2) is represented by a horizontal dashed line, and the standard deviation is indicated by a gray band. This value was obtained from the direct measurements carried out away from the vent field and is not to be confused with the basin background value of 175 mW/m^2. However, more distant measurements have not fully decayed to typical heat flow background values, suggesting convection takes place at a length scale much larger than observations. Note that transparent layers are consistent in all transects, including D-D' and E-E', which are parallel to the main fault directions (D, E). These zones have been interpreted as porous conducts saturated with fluids. Arrows indicate the position of heat flow values off scale. Sub-bottom profiles are plotted as a function of common depth point (CDP) versus travel time in seconds. Solid black and dashed lines represent faults and their continuation with depth, respectively. Vertical dashed lines represent the extension of the Auka vent field.

with a series of short spreading segments connected by long transforms and blanketed with terrigenous and biogenic sediment (Lonsdale & Lawver, 1980).

The nearest of these spreading segments to the Alarcón Rise is the 3,800 m deep Southern Pescadero Basin, 60 km NW along the Pescadero Transform Fault. It is one of three grabens offset by transform faults collectively named the Pescadero Basin and located 150 km east of La Paz, Mexico.

3. Structure and Stratigraphy of the Southern Pescadero Basin

The Southern Pescadero basin is a stretched sediment-filled graben bounded by relatively recent normal faulting (Figure 1B). It is a sigmoidal to rhomboidal, strongly asymmetric structural depression developed between the overlapping Alarcon and Pescadero transform faults (Figure 1B). A transverse system of sigmoidal faults in map view controls basin subsidence. These systems link the bounding transforms and transfer strike-slip motion into oblique-extensional motion (Figure 1B). The central portion of the basin, on the other hand, is characterized by a discrete array of east and west-facing sub-parallel normal faults forming a nested graben structure with an NNE-SSW orientation. Relay structures, such

Figure 1. (A) Simplified tectonic map of northwestern Mexico showing the boundary and relative motion between the Pacific and North American plates along the Gulf of California. This strongly transtensional plate boundary is characterized by an array of right-stepping, right-lateral transform faults connecting a series of pull-apart basins distributed along the Gulf's axis. Inset shows the location of the study area in the southern Pescadero basin. Abbreviations are as follows: EPR, East Pacific Rise; Tfz, Tamayo Fracture Zone; Afz, Alarcón Fracture Zone; Pfz, Pescadero Fracture Zone, (B) 40-m resolution bathymetry of the southern Pescadero basin showing the geometry of the overlapping Alarcon and Pescadero master transforms (in red), and the subsidiary shears that curve into a transverse system of oblique-extensional faults (black) controlling the subsidence of the basin. (C) 1-m resolution bathymetry of the central and western portion of the southern Pescadero basin, showing the diverse network of transverse faults and the location of the Auka and JaichMaa 'Ja'ag hydrothermal vent fields along the western wall of the structural graben. Insets show the location of heat flow measurements in the Auka and JaichMaa 'Ja'ag vent field. (D) Calculated heat flow values for the Auka and (E) the JaichMaa' Ja'ag vent field. Yellow dashed lines represent the spatial extent of vent fields in the area.

as intact and breached ramps, are also observed alongside the younger, innermost, fault scarp array. Sub-bottom profiles through the Southern Pescadero Basin suggest basement around rift shoulders at depths of less than 50 m (Figure 2). However, pre and syn-rifting sediment thickness appear to be much more significant across the rift-bounding faults. The western walls of the nested graben are controlled by a series of left-stepping, en-echelon faults. Fault length (up to ∼8.5 km) and vertical displacement (up to 175 m) increase westward systematically. The curved fault geometry suggests a more complex history of soft and hard-linking segment interaction. The recently discovered Auka and JaichMaa Ja'ag' hydrothermal vent fields cover areas ∼0.12 km^2 (75–150 m wide by 600 m long) and ∼0.05 km^2 (70–100 m wide by 400 m long), respectively, and lie along the trace of a fault striking N-S by ∼3 km (Figures 1C–1E). Paradoxically, longer faults to the west and north of the vent fields do not display signs of recent hydrothermal activity. Length-displacement scaling laws (Balsamo & Storti, 2010; Torabi & Berg, 2011) indicate that the fault displacement, D, for a fault this long, is $D \approx 20$ m, which roughly agrees with the morphology observed in the bathymetric data. Similar scaling relations between D and the width of the fault's damage zone, w, ($w \sim D$) constrain w to be no more than ∼10 m and its core to be no wider than ∼1 m (Balsamo & Storti, 2010; Torabi & Berg, 2011).

Little is known about the stratigraphy of the Pescadero Basin. Still, short cores recovered for paleoclimatic studies (e.g., Escorza-Reyes et al., 2013; Flores-Trujillo et al., 2009) suggest many similarities with sediments recovered by long cores in the Guaymas Basin (Barron & Bukry, 2007). It appears that the active rift-valley sediments consist primarily of a sequence of fine to very fine, poorly sorted, silty sand, interbedded with massive mass-flow deposits and hemipelagic diatomaceous oozes. These sediments have two distinct sources. Siliciclastics are supplied from fluvial, beach, and dune sources bordering the basin transported as a suspended load layer forming sheet-like sedimentary deposits in the basin floor. The diatomaceous oozes, by contrast, result from the steady deposition of biogenic production in the water column whose abundance correlates with eustatic sea-level changes (Barron et al., 2005).

4. Insights From Pescadero Basin Fluid Chemistry

The composition of hydrothermal fluids and precipitates at sediment-starved mid-ocean ridges is controlled by the temperature and pressure regime, the composition of source rocks, and volcanic volatiles inputs (Hannington et al., 2005; Monecke et al., 2016; Von Damm, 1990). Fluids can also react with rocks and sediments in the hydrothermal up-flow zone and provide information about the underlying hydrothermal systems, such as sediment involvement along flow pathways (Von Damm, 1990). In the case of the Auka vent field in the Pescadero Basin, the fluids' chemistry indicates extensive interaction with sediment, which necessitates the fluid upflow zones passing through a thick sediment blanket (Paduan et al., 2018).

The highest temperature measured in the Auka vent field was 291°C; however, supercritical phase separation and condensation of a high salinity brine point to temperatures above 400°C. The dissolved silica content of Auka fluids falls below the quartz saturation-line (Von Damm et al., 1991). Since silica solubility reverses at 375°C at the pressure of the Auka vents, it appears likely that the silica solubility reflects equilibrium at temperatures above 450°C at pressures determined by the depth of fluid circulation (Paduan et al., 2018).

Interestingly, Auka fluids have compositions similar to those from other sediment-hosted mid-ocean ridge vent fields, especially Guaymas Basin (Paduan et al., 2018). However, Guaymas chimneys contain abundant polymetallic sulfide in addition to hydrothermal calcite (Berndt et al., 2016; Von Damm, 1990), whereas the Auka chimneys are nearly pure calcite (Paduan et al., 2018). The $^3He/^4He$ ratio of 7.7Ra (multiple of present-day atmospheric $^3He/^4He$ ratio of 1.38×10^{-6}) reported by Spelz et al. (2015) indicates a dominantly mantle-derived source for helium; however, the nature of the basement rocks and extent of deep fluid circulation remains poorly constrained. Notwithstanding, carbon isotope values demonstrate that sediment interaction includes considerable carbonate dissolution in the subsurface. Carbonate is not preserved in surface sediment at the present depth of the basin, which suggests that substantial sediment accumulated prior to basin subsidence below the carbonate compensation depth. Moreover, the abundant carbonate deposits indicate that Auka is a long-lived vent field requiring extensive integrated water/rock reaction in the subsurface.

5. Heat Flow Measurements

We made 45 heat flow determinations (Figure 1d) using the instrument and procedure described in (see Figure S1). Table S1, lists the values of our new measurements and the thermal properties of sediments penetrated by the probe. The quality of heat flow determinations varies, but most measurements are of excellent quality (see supporting information for details). Nearly all heat flow sites display linear temperature-thermal resistance profiles suggesting conductive heat transfer or that if fluid flow is present, it is below detectable limits. Curvature in the temperature-thermal resistance profile was observed only at one station close to an active vent in the JaichMaa Ja'ag' field. Seepage only generates curvature in temperature thermal resistance profiles when the flow exceeds some minimum value that depends on probe length and other material parameters. For our probe specifications, the minimum velocity detectable is ~6 m/yr (see supporting information).

Heat flow values vary by approximately two orders of magnitude across the vent fields: from ~2 W/m^2, 500 m east of the Auka, to over 120 W/m^2 within the JaichMaa Ja'ag' vent field (see Table S1). Such high heat flow values are quite common throughout the Gulf of California rift system (e.g., Fisher & Becker, 1991; Neumann et al., 2017; Prol-Ledesma et al., 2013). By contrast, the thermal conductivity remains relatively constant throughout the basin, with observed values of 0.82 ± 0.08 W/m K (Table S1 and Figure S2).

Of the 45 measurements, 34 lie along three sub-bottom profiles (A-A', B-B', and C-C' the locations which are shown in Figures 1d and 2) obtained by MBARI's AUV. The AUV's sub-bottom profiler emits a 1–6 kHz sweep chirp pulse that travels through the water column into the sediment. Part of the energy is reflected by hard rocks or thick sand deposits, preventing the identification of stratigraphy and other structures, and part passes into the subsurface where the sediments are soft or unconsolidated. Based on the signal's intensity, an image of the subsurface is produced in the form of a two-dimensional (2D) cross-section, or sub-bottom profile (Figure 2), with penetration in sediment up to 50–80 m.

The heat flow measurement spacing along these profiles is nominally 100 m but decreases in areas of greater interest, that is, near faults and within the vent fields. Seven other measurements are scattered around the Auka vent field, and four more were acquired around the JaichMaa Ja'ag' field (Figures 1D and 1E). In Figures 2A–2C, we have plotted the heat flow data over sub-bottom profiles A-A', B-B', and C-C'. For clarity, we plot values at different scales, and we include a basic interpretation of the near-surface structures imaged by the sub-bottom profiles.

Figure 2A corresponds to the northern profile A-A' (Figure 1D) and shows that, away from the vent field, heat flow is ~2.2 W/m^2. The conductive flux increases toward the vent field, reaching a maximum of 72.6 W/m^2 at a normal fault bounding the eastern side of the vent field (Figure 2A). Fluctuations in heat flow are observed within the vent field for the northern profile. Figures 2B and 2C show the distribution of heat flow along the central and southern transects, B-B' and C-C' respectively. Heat flow has the same overall behavior observed in the northern transect (A-A') and analogous structural controls. In general, heat flow is relatively uniform away from the vent field but shows peaks where normal faults are present in the sub-bottom profiles (Figure 2). In the central transect (B-B'), heat flow values range from 1.1 W/m^2 to a maximum value of 34.3 W/m^2, whereas in the southern transect (C-C'), heat flow ranges from ~2 W/m^2 and a maximum of ~4 W/m^2 at the south tip of the Auka field (Figure 1D). Background heat flow of ~2.2 W/m^2 was estimated using the mean of the most distal heat flow values (dashed line in Figure 2). By contrast, the measurements in the JaichMaa Ja'ag' field show extreme local variability with a maximum of 123.7 W/m^2 and a minimum of 4.9 W/m^2. This variability is most likely due to hydrothermal circulation associated with the vent field.

Another interesting result in the sub-bottom profiles is the presence of seismically transparent layers in the basin sediments (Figure 2). Although the transparency could be due to poor imaging, the homogeneous texture of the material and distinct geometry is more typical of water-saturated sediment, possibly sand layers produced by density currents or siliceous oozes. If this is indeed the product of fluids, it implies the passage of large volumes of fluid from a source deep in the basin, along the normal fault, and through permeable layers in response to overpressure gradients acting at the Auka and JaichMaa Ja'ag' vent fields (Figures 2D and 2E). Moreover, supposing flow does occur in the way the sub-bottom profiles suggest, under the right conditions (e.g., Andersen et al., 2015) it would have the effect of making the basin hotter, explaining the slow heat flow decay observed in the data (Figures 2A–2C).

6. Hydrothermal Circulation Model of the Auka Vent Field

To better understand the hydrothermal circulation in the Auka field, we constructed a 2D model of the temperature distribution that includes fluid circulation in the basin sediments and preferential flow through a fault of finite width. The location of the model is across the fault zone and the Auka field, following the central profile (B-B') (Figure 2B). Because a purely conductive formulation is not reasonable, it seems to us that we need to incorporate advective heat flow into any potential model capable of explaining the heat flow measurements. A conceptual model for that system influenced by work carried out at Middle Valley (Davis & Becker, 1994; Fisher et al., 2008) is one in which a deep hydrothermal system is hosted within a permeable basaltic crust (Figure 3A). The basement is sealed by a sediment cap consisting of low permeability silt layers interbedded with permeable fine sand layers. Within this layering: (a) silt layers restrict the vertical circulation of fluids (e.g., Leon et al., 2017), which results in vertical conductive transport of heat through the basin sediments; (b) a permeable fracture system captured isolated upwelling plumes that vent geothermal brines through the seafloor; and (c) sand beds provide porous pathways for flow seepage parallel to the stratification allowing for extensive interaction with sediment (Figure 3B; Paduan et al., 2018). The result is the superposition of convective anomalies on the conductive heat flow background (Figure 3A). Large changes in sediment thickness and basal heat flow that could introduce fine-scale perturbations, appear to be unwarranted given the short lateral distances over which the heat flow measurements were collected (~1 km).

Figure 3 synthesizes in a schematic section our conceptual model of the Pescadero Basin hydrothermal system. As can be appreciated in that figure, our model consists of two subsystems, which we describe next.

6.1. Fracture Permeability Zone Model

^{3}He/^{4}He in water samples collected at the Auka and the JaichMaa Ja'ag' vent fields suggest a high-temperature thermal reservoir of basaltic composition drives fluid circulation (Paduan et al., 2018) in which the bounding fault's fracture permeability appears to localize the upflow of geothermal brines (Paduan et al., 2018; Spelz et al., 2015). Moreover, the geochemical evidence suggests that the vent field emission is substantial in terms of the mass of carbonate precipitated, and long lived, in which case it is reasonable to assume an approximate balance between the heat transported vertically within the fractured zone of finite thickness, w, the heat dissipated laterally by conduction, and the heat mined by circulation of hydrothermal fluids through permeable layers (Figure 3B). In other words, discharge has continued for a sufficient period of time to reach steady-state conditions. The balance of heat is expressed in the following relation (Figure 3B, modified from Lowell, 2017),

$$\rho_f c_f v_f w \frac{dT_f}{dy} = -2\frac{\lambda}{L}\left[T_f(y) - T_c(y)\right] - 2\rho_f c_f u_f\left[T_f(y) - T_c(y)\right], \quad (1)$$

where $T_f(y)$ is the temperature distribution inside the fractured (damage) zone and $T_c(y)$ is the conductive temperature (unperturbed) of the country-rock at some distance L away from the fault plane. ρ_f is the density of seawater, c_f its specific heat, v_f is the ascending velocity of the hydrothermal fluid, u_f is the horizontal seepage velocity of the fluid, and λ is the thermal conductivity of the country-rock. The left-hand side term represents the rate of heat transfer by venting (vertical advection), the first term on the right-hand side is the rate of heat transfer through the fault, and the second term on the right-hand side is the rate of heat transfer by seepage parallel to the stratification. This term is akin to Newton's law of convective cooling and the group constant $\rho_f c_f u_f$ plays a role similar to the heat transfer coefficient. The factor 2 in the last two terms in Equation 1 accounts for the heat lost through both sides of the fault.

A solution to Equation 1 is given by the expression (Lowell, 2017),

$$T_f(y) = \frac{T_0}{\mu h}\left[1 + \mu y - \exp\left(\mu\left(y - h\right)\right)\right]. \quad (2)$$

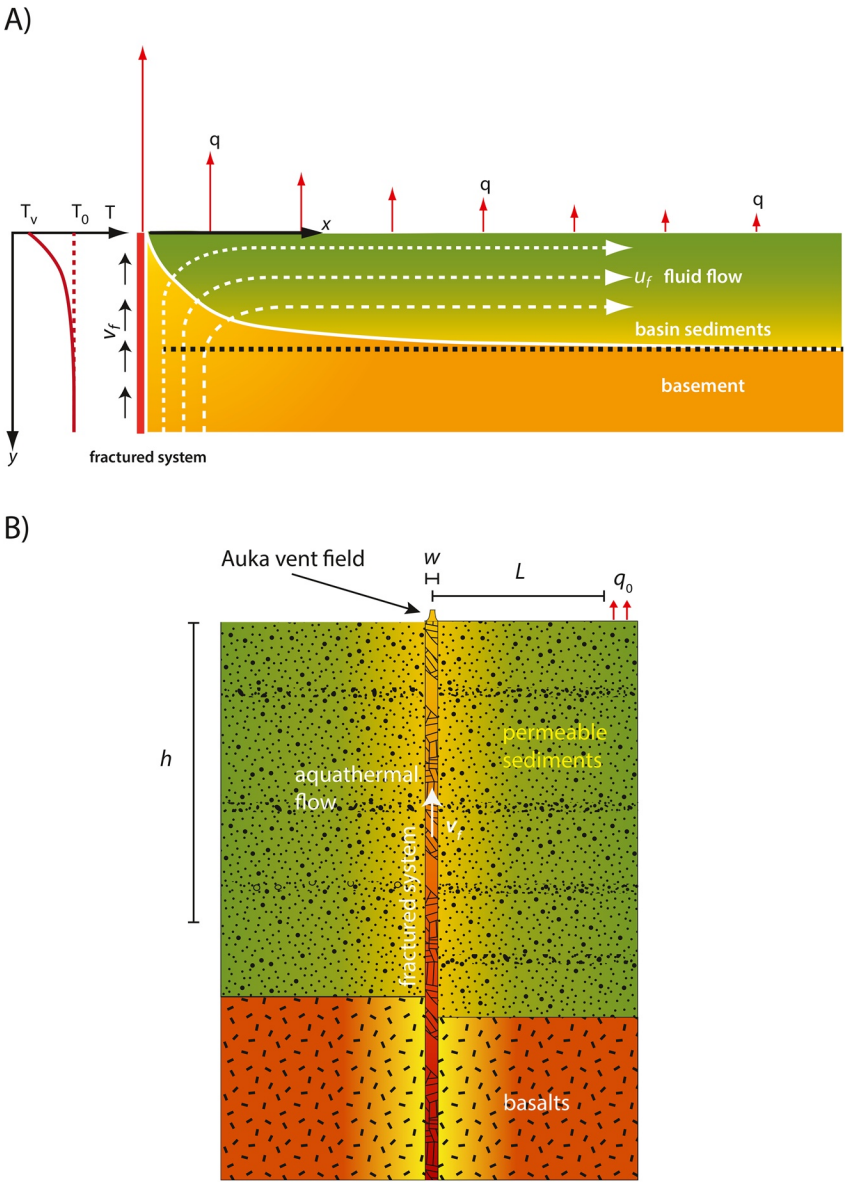

Figure 3. Conceptual model of the geothermal system of the Auka and JaichMaa Ja'ag' vent fields in the Southern Pescadero Basin. (A) Diagram illustrating the dissipation of heat through the fault wall to the sediments filling the hanging wall block of the central graben. In our view, permeable pathways (i.e., faults) provide advective flow and result in anomalies superimposed on the conductive background heat flow of the basin. Near the fault (left vertical boundary) heat is mostly transported vertically causing uplifting of the isotherms, while heat in the basin is slowly advected horizontally by flow parallel to the sedimentary beds and dissipates vertically by conduction. (B) Sketch of the geothermal source and fractured zone. w is the width of the fractured zone, h is the depth to the heat source, and q_0 is the conductive heat flow dissipated by the source.

To obtain (2), we used the boundary condition: $T_f\left(h\right) = T_0$, where T_0 is the temperature of the geothermal reservoir and h is the depth of the reservoir. Note that y is positive downwards (Figure 3). Also note that the ratio $T_0 \,/\, h$ in Equation 2 is connected to the steady-state heat flow q_0 produced by the geothermal reservoir at a temperature T_0 through Fourier's Law,

$$q_0 = \lambda \frac{T_0}{h}. \tag{3}$$

In expression (2) $1/\mu$ is the characteristic advection length scale of the system given by

$$\frac{1}{\mu} = \frac{\rho_f c_f v_f w\, h}{2\Lambda}. \tag{4}$$

In this last expression, we have assumed that $L \approx h$ (Lowell, 2017) and Λ represents an enhanced thermal conductivity caused by the convective cooling through the fault

$$\Lambda = \lambda\left(1 + Nu\right), \tag{5}$$

where $Nu = h\rho_f c_f u_f \,/\, \lambda$ is the Nusselt number, the ratio of heat transported in a convecting layer to that which would be transported by conduction alone (Davis et al., 1997). This agrees with modeling results by the previous authors, whom found that the heat transported by fluid motion in sediment-buried igneous oceanic crust can be modeled accurately by enhancing the thermal conductivity. The factor by which conductivity is enhanced above the true conductivity being a proxy for the Nusselt number (Davis et al., 1997).

6.2. Basin Heat Flow Model

The vent's fluid chemistry indicates extensive interaction of fluids with sediment, including a lot of carbonate dissolution in the subsurface (Paduan et al., 2018). This hints that the upflow zones pass through a thick sediment blanket and/or, possibly, circulates within permeable sediment layers in the basin (Figure 2). We interpret the observed pattern of Figure 2 reflecting a combination of vertical heat advection within the permeable fault zone relayed by diffusion, as well as advection by hydrothermal fluids that circulate throughout the basin. Given the extremely low permeability ($\sim 10^{-17}$ m^2) and good stratification of hemipelagic sediments, we assume the flow to be stable and parallel to the stratification. These assumptions appear to be warranted in light of (a) the heat flow measurements covering a very small area within ca. 1 km radius from the vent field axis, and (b) the complete convection cell, if present, appears to be on the order of several kilometers so that at the measurement's length scale, flowlines are essentially horizontal (Figure 2).

Assuming steady-state and negligible internal heat generation, we expect the heat drawn out through the fault wall by advection to be balanced with the heat dissipated vertically through the sediments accumulated in the hanging-wall block,

$$u_f \frac{\partial T_b}{\partial x} = -\kappa \frac{\partial^2 T_b}{\partial y^2}, \tag{6}$$

where T_b is the temperature distribution within the basin, u_f is the flow velocity in permeable layers in the horizontal direction, and k is the thermal diffusivity. The thermal diffusivity is given by $k = \lambda / c_f \rho_f$. As can be appreciated, the model lacks buoyancy forces to set the fluid in self-sustained convection, though later on, we establish a connection between u_f and buoyancy forces. In a sense, this is akin to Parsons and Sclater (1977) lithospheric plate cooling model, which is a purely kinematic model. A variety of alternative scenarios that also consider restricted flow paths will be further analyzed in the discussion section.

To find a suitable solution to this partial differential equation (PDE), we need a set of appropriate boundary conditions. Naturally, the temperature T_b inside the basin needs to satisfy the temperature of the fractured zone (temperature continuity)

$$T_b\left(0, y\right) = T_f\left(y\right). \tag{7}$$

Another boundary condition we consider is an isothermal water-sediment interface

$$T_b\left(x > 0, y = 0\right) = 0°\text{C}. \tag{8}$$

Here, we consider that the thickness of the fracture zone w is small, in the order of 1 m or so, and is approximated by a heat line source at $x = 0$. As we demonstrate in the supporting information, this problem can be expressed as the superposition of two thermal processes $T_b = \psi\left(x, y\right) + \phi\left(x, y\right)$ (e.g., Carslaw & Jaeger, 1959). $\psi\left(x, y\right)$ represents the sum effect of a series of constant line sources concentrated at the vent

field ($x = 0, y > 0$), whose temperature decays exponentially with distance, and the deep heat flow coming from the top of the reservoir. $\phi(x,y)$ represents a heat flow perturbation brought about by advection along the fractured system. In the supporting information, we derive closed-form expressions for these functions and demonstrate that the resulting steady-state temperature field is given by the following expression (see Equation S14 and S19)

$$T_b = \frac{T_0}{\mu h}\left[erf\left(y\sqrt{\frac{u_f}{4\kappa x}}\right) + \mu y\right] + \frac{T_0}{\mu h}\frac{A}{2}\exp\left(-\mu y + \frac{\chi\mu^2 x}{u_f}\right) \left[erfc\left(\frac{y - \left(2\chi\mu x / u_f\right)}{2\sqrt{\chi x / u_f}}\right) - \exp\left(2\mu y\right) erfc\left(\frac{-y - \left(2\chi\mu x / u_f\right)}{2\sqrt{\chi x / u_f}}\right)\right], \quad (9)$$

where $A = \exp(-\mu h)$. In Figures 4A–4C, we have plotted $\psi(x, y)$, $\phi(x,y)$, and the steady-state temperature field $T_b(x, y)$ predicted by the model using the parameter values listed in Table 1. As we can see, $\psi(x, y)$ (Equation S14) is the solution of the cooling of a lithospheric plate (e.g., Parsons & Sclater, 1977; Figure 4A), which results in the development of a boundary layer along the water-sediment interface, whereas $\phi(x,y)$ is a negative valued function (Figure 4B), which causes $T_b(x, y)$ to curve with depth as a result of the upward transport of fluids along the fault plane (Figure 4C).

From the derivative of T_b (Fourier's Law) and setting $y = 0$, we can obtain the heat flow across the water-sediment interface (see Equation S21)

$$q_b = \lambda\frac{T_0}{\mu h}(1 - A)\sqrt{\frac{u_f}{\pi\kappa x}} + \lambda\frac{T_0}{h} - \lambda A\frac{T_O}{h}\sqrt{\frac{u_f}{\pi\kappa x}} \times \exp\left(\frac{-h^2}{4\chi\left(x / u_f\right)}\right). \quad (10)$$

In the Supporting Information, we discuss the scaling properties of our model in terms of the characteristic length scale of diffusion, w, h, and the Rayleigh number.

6.3. Parameter Extraction Using Least Squares Inversion

Equations 2, 4, 9 and 11 contain parameters with important information about the Auka hydrothermal field in the southern Pescadero Basin. The depth to the source is included in h; the intensity of the convection in the fractured zone is embodied by v_f and μ; The thermal state of the geothermal system is represented by T_0 and λ/h. In the following paragraphs, parameter extraction is performed from the heat flow measurements to estimate these and other properties.

To establish the depth of the geothermal source, we need information about the temperature of the geothermal reservoir T_0 and its background heat flow q_0. The hydrothermal water chemistry suggests the former parameter is on the order of 500 ± 100°C, whereas heat flow measurements in the Guaymas Basin, Central Gulf of California, show that an acceptable value for the latter is 175 ± 25 mW/m^2 (Becker & Fisher, 1991; Williams et al., 1979). Substituting these values in Equation 3 and assuming a thermal conductivity $\lambda = 2$ W/m K that is, more representative of the upper crust (0–20 km) than our near-surface values, the geothermal reservoir depth is $h = 5.7 \pm 1.4$ km.

Next, the convective length scale $1/\mu$ provides information on how vigorous convection is with respect to conduction in the fractured system. To estimate the intensity of this phenomenon, we substituted (3) in (2), set $y = 0$, and derived the following relation,

$$\frac{q_0}{\mu\lambda}\left[1 - \exp(-\mu h)\right] - T_v = 0. \quad (11)$$

This is a root-finding problem that can be easily solved by utilizing the bisection method. The only unknown parameter in Equation 11, other than the convective length scale μ, is the temperature T_v of the hydrothermal fluids exiting the vents. The ROV measured the temperature of fluids discharging from the vents during the dives, obtaining a value for $T_v = 291$°C (Table 1). Based on the values above, the bisection

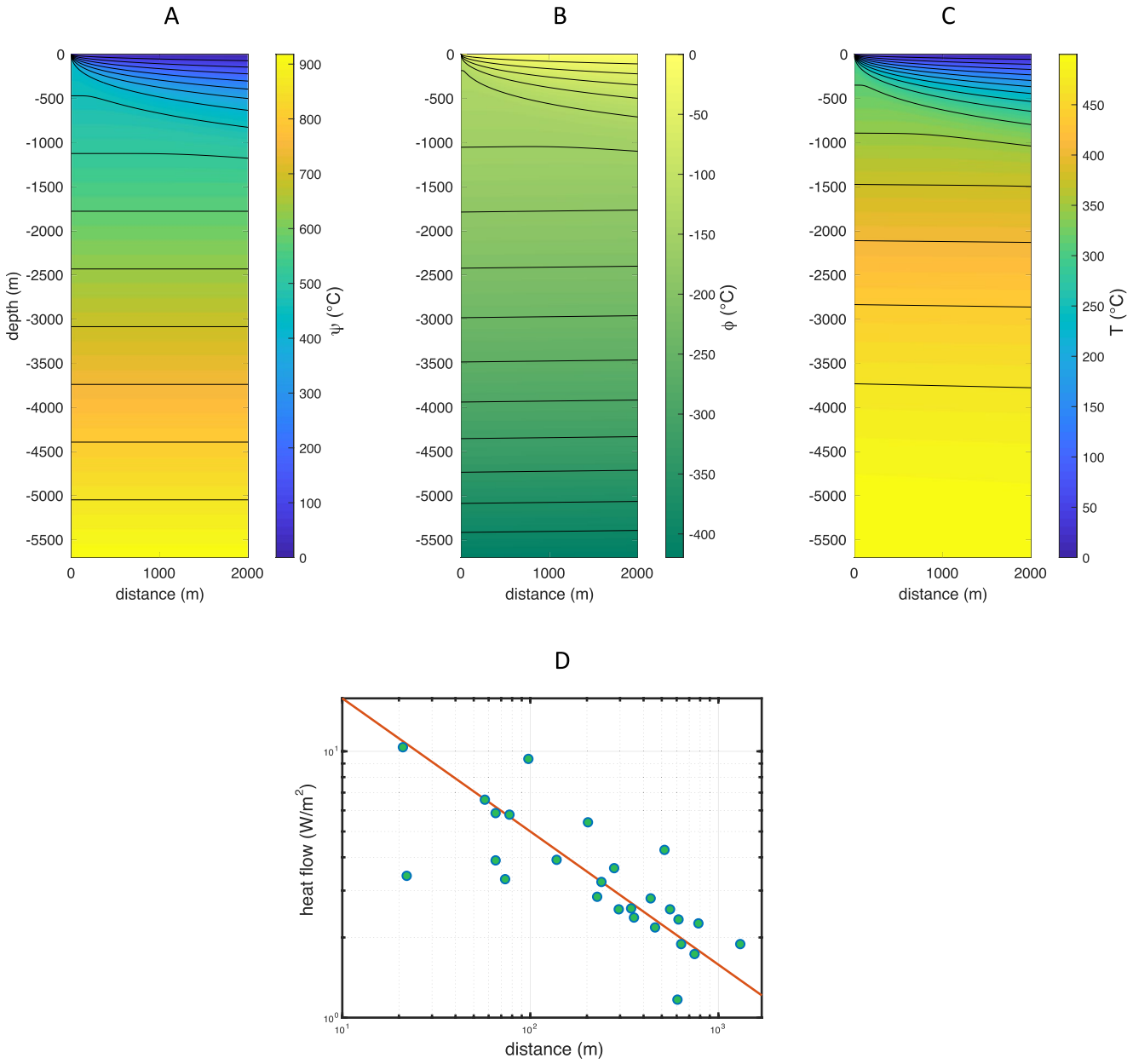

Figure 4. (A) Temperature distribution of the function $\psi(x,y)$ described in the main text and supporting information. (B) Temperature distribution of the function $\phi(x,y)$ described in the main text and supporting information. (C) Model of the temperature distribution of the Auka vent field and sedimentary basin given by $T(x,y) = \psi(x,y) + \phi(x,y)$ using the parameters listed in Table 1. See Equation 9 in the main text and supporting information. Observe how the temperature changes rapidly in a narrow layer around the isothermal seafloor. (D) Log-log plot of the heat flow measurements acquired in the Auka vent field. Red line is a best-fitting curve with a slope $-1/2$, suggesting that the heat flow decays following an inverse square-root of distance power law, $q_b \sim x^{-1/2}$.

method yields a characteristic advection length scale $1/\mu \sim 4.8$ km that strongly dominates over conduction, as expected. In the calculation, we have used a reduced value for the thickness of the damage zone $w = 1$ m, as per fault growth scaling laws in soft sediments (Balsamo & Storti, 2010).

Before obtaining the upward flow velocity within the fractured system, first we need to obtain the horizontal seepage velocity through the fault u_f (Figure 3B). We used a least squares fitting method between the observed heat flow and Equation 10 to obtain the best possible estimate of this parameter (Figure 5). Observe, however, that since the exponential term in Equation 10 vanishes for values of $h^2 / 4\kappa(x / u_f) \gtrsim 6$, then

Table 1
Model Parameters

Parameter	Symbol	Mean value	Uncertainty	Units
Width of the high permeability fracture zone	w	1[a]	±0.5	m
Vent's temperature	T_v	291[b]	±1	°C
Geothermal reservoir temperature	T_0	500[b]	±100	°C
Background heat flow	q_0	175 [c]	±25	mW/m^2
Thermal conductivity	λ	2.0[e]	–	W/K m
Coefficient of thermal expansion	α	10^{-3} [e]	–	°C^{-1}
Thermal diffusivity	κ	10^{-6}[e]	–	m^2/s
Density	ϱ_f	1000 [d]	–	kg/m^3
Specific heat	c_f	4.2×10^3[e]	–	J/kg/°C
Depth to the source	h	5.7	±1.4	km
Upward fluid velocity	v_f	8.00×10^{-7}	$\pm 5.89 \times 10^{-7}$	m/s
Horizontal seepage velocity	u_f	1.86×10^{-8}	$\pm 9.22 \times 10^{-9}$	m/s
Permeability of the fractured system	k_f	1.62×10^{-14}	$\pm 1.24 \times 10^{-14}$	m^2
Pelagic sediments permeability	k_b	3.79×10^{-16}	$\pm 2.03 \times 10^{-16}$	m^2
Convection length scale of the fractured system	μ	2.10×10^{-4}	$\pm 1.02 \times 10^{-4}$	m^{-1}
Viscosity	ν	10^{-7} [e]	–	m^2/s

[a]Balsamo and Storti (2010). [b]Paduan et al. (2018). [c]Williams et al. (1979); Becker and Fisher (1991). [d]Wagner and Kretzschmar (2007). [e]Lowell (2017).

the first two terms should be dominant at the length scale of the observations ($x \lesssim 10$ km). Thus, during the inversion, we only considered the following simplified expression,

$$q_b = \lambda \frac{T_0}{\mu h} \frac{1 - A}{\sqrt{\pi \kappa x \,/\, u_f}} + \lambda \frac{T_0}{h}, \tag{12}$$

which predicts the heat flow to decay following a $x^{-1/2}$ power law (Figure 4D). Assuming a thermal diffusivity of $k = 10^{-6}$ m^2/s, the value u_f that best fits the superficial heat flow observations is $u_f = 1.9 \times 10^{-8}$ m/s. From this value we obtained $Nu \approx 200$, which is characteristic of very high Rayleigh number convection regimes (Davis et al., 1997); thus, the fracture zone cools predominantly via seepage through the fault walls. Then, we proceeded to obtain Λ using relation (5) and, by substituting Λ in relation (4), an upward flow value $v_f = 2.82 \times 10^{-8}$ m/s is obtained. The value of v_f appears low for a vent, but perhaps this and the high Nusselt number, explain why the fluids cooled ~200°C from their reservoir temperature (Paduan et al., 2018). Based on these flows and the parameter values listed in Table 1, we constructed the 2D temperature distribution and superficial heat flow models of the Auka vent field shown in Figures 4C and 5.

Since we know the flow velocities, both in the fractures and basin sediments, we obtained their permeabilities from Darcy's Law (see Equation S22). Using a value for the coefficient of thermal expansion $\alpha = 10^{-3}$°C^{-1} and a kinematic viscosity $\nu = 10^{-7}$ m^2/s for water, one obtains that the fractured system permeability is $k_f \sim 10^{-14}$ m^2. By contrast, the permeability of the basin sediments is $k_b \sim 10^{-16}$ m^2. The basin sediment permeability is in accordance with the permeability of hemipelagic sediments (Spinelli et al., 2004). However, we point out that the value derived here more likely represents an average of the layering aggregate as a whole rather than being representative of high permeability layers only. The fracture permeability, on the other hand, appears to be on the low side of values reported for faults and is low for the values observed for vents (Curewitz & Karson, 1997).

Based on the previous values and those listed in Table 1, we find the Rayleigh number of the damage zone is $Ra_f \approx 10^3$ (see supporting information for details). This value indicates the fracture system is under vigorous convection (Davis et al., 1997) in which nearly vertical columnar plumes control the heat transport as the

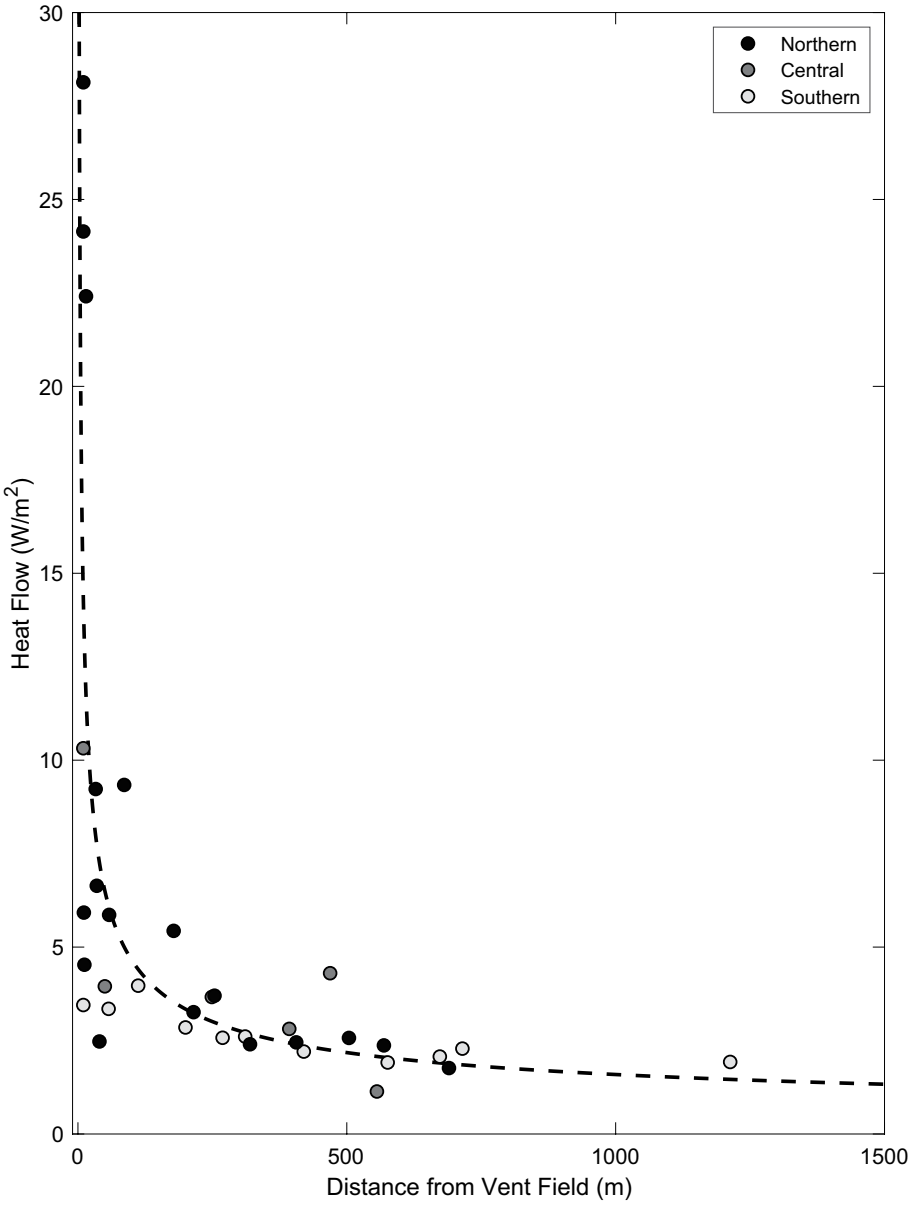

Figure 5. Results from the least square fitting between the observed data and the predicted heat flow described in Equation 12 using the best estimates for μ and h. Observed heat flow values from the three transects across the Auka field (grayscale circles) and predicted heat flow (dashed line) are plotted vs. distance, to the center of the vent field.

convective time scale is much shorter than the conductive time scale. By contrast, the Rayleigh number Ra_b in the basin sediments is roughly a factor of two the critical Rayleigh number for the onset of convection in a porous media ($Ra_b \approx 10^2$), and circulation in the basin could be in the form of weak, steady convective rolls. Given that Rayleigh convection is energetically most favorable to equidimensional cells, it is likely that the cell length is in the order of the depth of the thermal reservoir or ~6 km.

7. Discussion

7.1. Scaling Relationships

The model for steady hydrothermal circulation is conceptually very simple, yet it explains quite well the heat transfer observed at the Auka hydrothermal vent field and basin interior (Figure 4). A basic prediction of the

model is that the superficial heat flow should decay asymptotically with distance following an $x^{-1/2}$ power law. Results showed a high similarity between the prediction and field data (Figure 4D). Furthermore, this underlying trend puts relation (2) in a solid footing as, often, equilibrium is approached asymptotically.

The $x^{-1/2}$ power law observed in the data frequently appears in flow problems around an isothermal surface in which heat exchange between the flow and the surface gives rise to a thermal boundary layer whose thickness is controlled by the diffusion length scale $\delta = \kappa / u_f = h / Ra_b$ (e.g., Landau & Lifshitz, 1987; Figure 4C; see also the supporting information). In these circumstances, the isothermal plane is the water-sediment interface, slightly above 0°C, whereas the flow is the seepage of hot springs parallel to the stratification. Observations also indicate that the boundary layer grows until it becomes unstable at some critical distance x_c, sinking rapidly forming a convection roll. The length scale of the convection roll scales inversely with the Rayleigh number (see Lowell & Germanovich, 2004). So, if we decrease Ra, say by reducing the permeability, this would have the effect of stabilizing the boundary layer over longer distances, which could explain the slow decay observed in the Auka data and the elevated background values of ~2 W/m^2 at distance of ~1 km from the fault. In the light of this cursory discussion, it appears our model is a near fault approximation ($x < x_c$) valid for the limiting case of heat transport in a low Rayleigh number convective regime.

Analytical scaling relations in our model reveal the heat flow scales as $q_b \sim T_0 \Gamma \delta^{-3/2}$, where $\Gamma = wk_f / k_b$ is the relative fault transmissivity (see the supporting information that accompanies this study). Andersen et al. (2015) have shown that the latter parameter is crucial for maintaining the delicate energy flux balance required for the formation of a vent. The scaling law, however, is only valid for small faults. One could expect faults with a larger displacement, and thus longer faults, to be more efficient in transporting heat as Γ scales with fault displacement, D, given $w \sim D$, but in soft sediments that conjecture is not necessarily true.

First, the permeability of the damage zone in siliciclastic sediments scales inversely with displacement $k_f \sim D^{-1}$ due to a reduction in porosity by grain shearing (Balsamo & Storti, 2010), whereas the width of the damage zone scales as $w \sim D$ (Torabi & Berg, 2011). Thus, these two effects cancel each other out, and in fact Γ might even decrease for fault displacements greater than 25–30 m (Balsamo & Storti, 2010). Incidentally, this might be one of the self-adjusting, pore space-clogging mechanisms suggested by Andersen et al. (2015) that help sustain vent activity over long timescales. Second, it is possible to show that an intrinsic relationship must exist between permeability, seepage of heat through the fault's walls, and upflow temperature. We deduce this from conservation of heat arguments. If we consider the heat flow across the fault, q_f, scales in a negative fashion as $q_f/w \sim q_b/h$, then heat flow in the damage zone must decrease as $q_f \sim w^2 \delta^{-3/2} k_f / hk_b$. Furthermore, the temperature drop in the damage zone scales as $w^3 k_f$. The conclusion is the higher the permeability and the wider the damage zone, the higher the loss of heat, and the lower the vent temperature (Andersen et al., 2015).

The scaling relationships discussed above elucidate the mechanisms of formation of the Auka and Jaich-Maa Ja'ag' fields and explain why other longer neighboring faults do not show signs of hydrothermal activity (Figure 1c). In the heterogeneous crust of the Pescadero Basin, a minor fault appears to have captured two isolated upwelling plumes formed in the fine-grained sediments at the southern terminus of the basin. Scaling laws suggest that only faults <3 km in length appear to develop the conditions required to sustain the observed temperature gradients. If that is, the case, the relative transmissivity of the fault's damage zone is the strongest control on the width of the captured plume, and therefore on the heat flow decay length. The fault could also, in theory, host both hydrothermal recharge and discharge by lateral circulation along the fault plane strike.

7.2. Model Limitations and Advantages

Data collection in marine environments is an activity inherently limited and one of the great advantages of the model presented here is that it provides simple relationships to estimate the parameters that characterize the convective state of a hydrothermal system from heat data alone. As we have demonstrated, parameter extraction from the model is a straightforward procedure that requires basic fitting and root finding

techniques. In contrast, the procedure remains cumbersome in nonlinear dynamic models due to nonconvexity, parameter sensitivity, and high computational cost. At the same time, there are simplifications in the two models presented in Sections 6.1 and 6.2. To get the vertical temperature profile in the high-permeability damage zone (Equations 1 and 2), it is assumed that heat is lost convectively and conductively over a horizontal length scale $L \approx h \approx 5$ km (Lowell, 2017). Then, the temperature field in the sedimentary basin is obtained through Equation 9 assuming continuity in the temperature field and horizontal seepage flow across the fault. Notice that in Equation 1 mining of heat by conduction is approximated by a temperature difference instead of its derivative. This approximation is necessary because the boundary conditions (7) and (8) include a Dirac-delta-type singularity at the origin ($T_b\,(y=0, x=0) = 290°\text{C}$, $T_b\,(y=0, x>0) = 0°\text{C}$) to account for the sudden increase in superficial temperature at the vent. Thus, the derivative of the temperature diverges at the origin and the problem is intractable (see Equations S15 and S16). This is true even for numerical methods as solving a problem with the aid of a computer does not change the intrinsic nature of the mathematical problem. Instead, a modified mathematical problem to alleviate the singularity is usually solved, which gives accurate results for relatively coarse meshes at relatively close distances.

The emergence of a singularity in the analytical solution is a well-known mathematical pitfall that emerges in many boundary-value problems in solid, fluid, thermal conduction, and fracture mechanics (e.g., Cole et al., 2010; Crouch et al., 1983). With hindsight, perhaps the presence of the singularity and the lack of data is why Lowell (2017) resorted to the rather simple regularization of the energy flux across the fault wall, approximation that we have adopted and further extended in this work. Though, to be fair, it appears to be warranted since the thermal plume cools down to a large extent by venting through the seafloor and horizontal convection of heat through permeable layers ($\text{Ra}_f \approx 10^3$, $Nu \approx 200$).

In Figure 6A, we have plotted the temperature field of a naturally convecting fluid in an isotropic, homogeneous porous medium. The solution was obtained solving numerically the conservation of mass, energy and momentum equations using the finite-differences numerical scheme developed by Olive and Crone (2018) (https://github.com/tjcrone/multiporo). The numerical simulation utilizes a constant basal temperature $T(x, y=h) = 500°\text{C}$, and a uniform temperature $T(x, y=0) = 0°\text{C}$ at the water-sediment interface. The simulated sedimentary layer has a thickness of 5 km and a permeability of 10^{-16} m^2, forming a sealed convective system (zero mass flux at the top and bottom of the layer). The porosity of the layer is 15%; all other material parameters like thermal conductivity, thermal diffusivity, density, etc., are the same for both models (Table 1). An important difference is that the properties of the convecting fluid (viscosity, density, etc.) are function of pressure and temperature and are calculated at each time step using a thermodynamic lookup table. As can be appreciated in Figure 6B, models have similar superficial heat-flow- decay length scale and roughly comparable heat flow amplitude at the center of the plume. In Figure 6C, we have further plotted the flow velocity along the x-direction and notice that the average velocity $\sim 2.5 \times 10^{-9}$ m/s is about a factor of four slower than the constant flow velocity u_f predicted by our model (Table 1).

However, when the numerical predictions are compared with the field data, a poor fitting is observed (Figure 6D). The numerical solution decays more rapidly than the heat flow data, following a law of the form e^{-x^2}, whereas our analytical solution does a better job in fitting and reproducing the overall trend in the experimental data. The reason is the numerical solution does not incorporate the Dirac-like discontinuity at the origin. In the numerical simulation the temperature along the top boundary is held constant at $T_b\,(z = 0, x) = 0°\text{C}$ and for that reason, a thermal layer of finite thickness $\delta \sim \left(\kappa h / v_f\right)^{-1/2}$ (e.g., Contreras & Negrete-Aranda, 2014) forms directly above the plume head. When the layer is advected laterally by the turning upwelling flow, it diffuses and expands following the well-known solution of the cooling of a layer of finite thickness (Carslaw & Jaeger, 1959, Equation 4) and the heat flow decays exponentially with distance.

7.3. Model Parameters

The permeability and flow rate in the fractured system and basin sediments are consistent with permeabilities estimates reported in sediments in the GC (e.g., Morin & Silva, 1984; Spinelli et al., 2004). Denlinger and Holmes (1994) estimated, using a thermo-mechanical model for sediment hills along the Escanaba Trough, an average fluid velocity (7.5×10^{-6} m/s) and a permeability (3×10^{-13} m^2) for a 2 m wide fracture zone

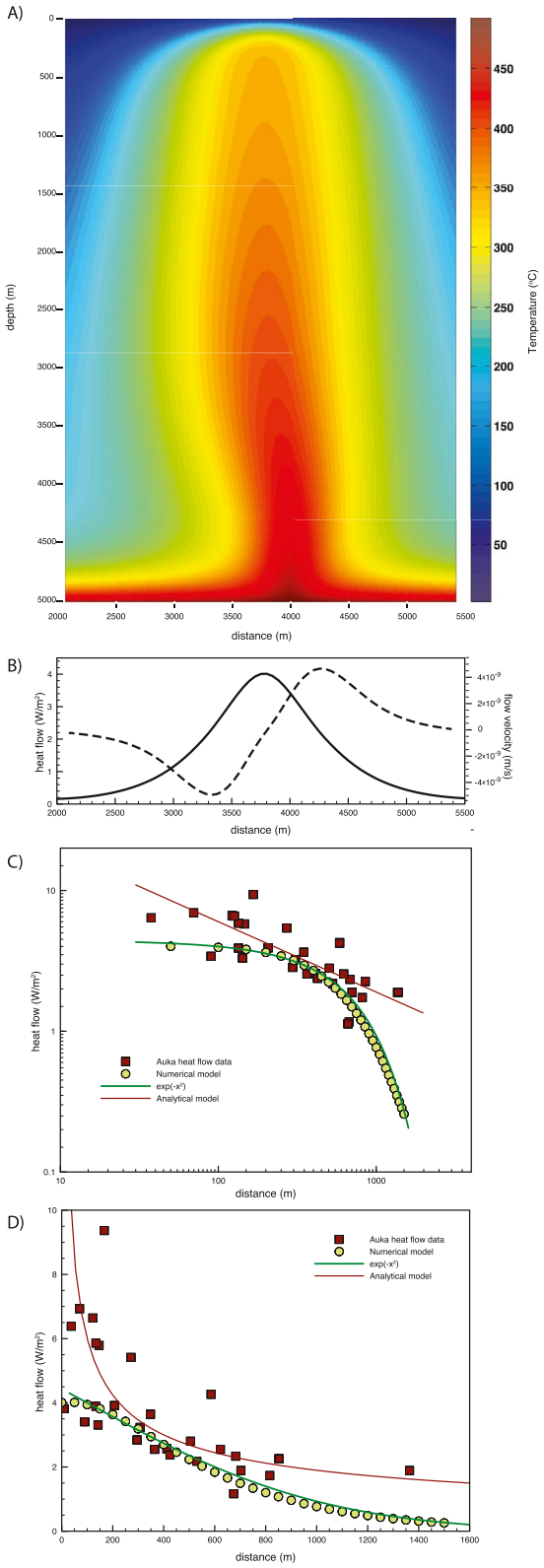
A)
depth (m)
distance (m)
Temperature (°C)
B)
heat flow (W/m²)
flow velocity (m/s)
distance (m)
C)
heat flow (W/m²)
Auka heat flow data
Numerical model
exp(-x²)
Analytical model
distance (m)
D)
heat flow (W/m²)
Auka heat flow data
Numerical model
exp(-x²)
Analytical model
distance (m)

Figure 6.

both are an order of magnitude higher than our estimates for a 1 m wide fracture zone. Davis et al. (1999) reported lateral flow rates at the Juan de Fuca Ridge of $\sim 1.5 \times 10^{-8}$ m/s. These are in good agreement with results obtained from our model though the lateral flow in the Juan de Fuca Ridge occurs in the basement under an impermeable sediment layer (Table 1).

Our model predicts a pattern of hydrothermal circulation that is, fast and vertical on the fault zone and slower and horizontal throughout the sediment produced by a source that is, quite deep ($h \approx 5$ km), perhaps a dominantly mantle-derived source. Since no seismic surveys capable of imaging sills have been conducted in the Pescadero Basin, the nature of the basement rocks and the extent of deep fluid circulation remain uncertain. Despite the lack of imaging, geochemical clues corroborate model predictions. Vent fluids display $^{3}He/^{4}He$ consistent with interaction with basaltic to ultramafic rocks that are probably the heat source driving high-temperature fluid circulation (Spelz et al., 2015). At the same time, the slow motion of fluids in the basin sediments ($u_f \approx 10^{-8}$ m/s), which presumably increased the fluid path length through the sediments, explain extensive fluid-sediment interaction in the Auka fluids (Paduan et al., 2018). In the configuration shown in Figure 2, the fluids interacting with the sediment move away from the vent field and are not sampled by the fault. But as the sediment fluids are being drawn in by the return flow they get hotter consistent with the heat flow and interact with the sediment and then are sampled by the fault.

The potential role of sills in controlling vents at Pescadero needs to be tested by seismic studies and drilling. Still, our modeling suggests sills are not required, and there are no geologic (or geophysical) observations at the Pescadero vent fields suggesting the presence of sills associated with the two-known high-temperature vent fields. Paduan et al. (2018) do point to two uplifted sediment hills, the southernmost of which is associated with temperature anomalies in the water column, but neither of which are known to have associated hydrothermal deposits.

7.4. Comparison With Other Vent Fields in the Pacific

We now explore some of our work's implications with relation to observations in similar environments along the Pacific plate boundary and the balance and distribution of heat in sediment-hosted vent fields. Although the fault model seems appropriate and straightforward for the Pescadero vents, it does seem to be the exception compared to other known sediment-hosted vent fields in the Pacific, which require entirely different boundary conditions than those observed in the Pescadero Basin. Convection at ridge flanks usually is sealed off from the ocean by a layer of fine-grained sediments of the deep ocean which typically have a permeability much lower than that of the upper volcanic crust resulting in little fluid exchange through seafloor sediments (e.g., Farahat et al., 2017; Fisher & Wheat, 2010). In this model, seamounts play a fundamental role in facilitating the exchange of fluids, heat, and solutes between the oceanic lithosphere and the overlying ocean by providing pathways for discharge and recharge. By contrast, convection in the heterogenous crust of the southern Pescadero Basin involve thermal upwellings captured by faults, much like what is envisioned at ridge flanks with faults instead of seamounts, and long cells with large portions of horizontal flow along permeable layers (perhaps coarse-grained mass-gravity deposits or siliceous oozes) allowing for the transference of solutes between sediments and vent sites.

Most of the high-temperature hydrothermal systems at sediment-covered spreading centers seem to be associated with faulted margins of sediment hills uplifted over large sills emplaced at the sediment-basalt interface. Examples include Bent Hill at Middle Valley (Zierenberg et al., 1998) and Central Hill at Escanaba Trough (Denlinger & Holmes, 1994; Zierenberg et al., 1993, 1998), and possibly some older dead deposits in the Northern trough at Guaymas (Lonsdale & Lawver, 1980). Most of the active vents in Guaymas Basin, and some small deposits at SESCA in Escanaba Trough, are associated with the edges of sills emplaced at relatively shallow depths in the sedimentary cover (Lonsdale & Becker, 1985; Peter & Shanks, 1992). In

Figure 6. (A) Numerical solution of the formation of a thermal plume in a homogeneous porous medium. Model's material parameter and geometry are as those listed in Table 1. The simulation considers a homogenous temperature at the top boundary of 0°C. (B) Superficial heat flow anomaly produced by the thermal plume (solid line) and horizontal flow velocity at a depth of 250 m (dashed line). (C) Log-log plot comparing the superficial heat flow of the numerical model shown in (A), our analytical solution (Equation 12), and Auka vent field heat flow measurements. Notice that the analytical solution fits better the overall trend in the data. (D) Same plot as in (C) using linear scales instead of logarithmic. Notice that the fit between the numerical solution and heat flow data is particularly poor near the fault and for far-field values.

these cases, the fluids still seem to be basement-derived (and heated) fluids, as opposed to being driven by the sills' heat. The vents' location above the sills' edges suggests the sills are impermeable aquicludes that force upwelling fluids to flow laterally until they can rise to the surface beyond their edges.

In some other environments, like the Dead Dog vent field studied during IODP Leg 169, upflow is located above a buried basement high (seamount), which forms a permeable chimney extending partway through the relatively impermeable sediment cap (Zierenberg & Miller, 2000). One exception is a small vent named Puppy Dog at Middle Valley, near Drill Hole 857D, a 1 m in diameter cluster of tubeworms surrounding a 202°C vent, that also seems to be associated with a very small fault (Cruse et al., 2008).

8. Conclusions

We made 45 new heat flow determinations in seafloor sediments of the Pescadero Basin around the newly discovered Auka and JaichMaa Ja'ag' vent fields using a 60 cm long probe integrated with ROV SuBastian (Figure 1). The measurements are spaced ∼100 m apart and are of excellent quality as nearly all heat flow sites display linear temperature-thermal resistance profiles. The conductive flux increases toward the vent field, reaching a maximum of 72.6 W/m^2 at a normal fault bounding the vent field to the east and decays away from the vents following an inverse square-root of distance law to a value of ∼2.2 W/m^2. This power law is typical of flow problems around an isothermal surface (Landau & Lifshitz, 1987) in which heat exchange between the flow and the surface gives rise to a thermal boundary layer whose thickness increases as the square root of distance (Figure 4D).

We developed an analytical model for the limiting case of heat transport in the vicinity of a fault in a low Rayleigh-number convection regime. The model accounts for the mining of heat across the fault's damage zone by seepage parallel to the stratification and by conduction. The model explains quite well the heat flow observed at the Auka hydrothermal vent field up to a distance of ∼1 km from the fault (Figure 5) but breaks down for large distances. The analytical approximation converges to more general numerical solutions based on the conservation of mass, energy and momentum.

It predicts a pattern of hydrothermal circulation that is fast and vertical on the fault zone and slower and horizontal throughout the sediment produced by a source that is, ≈5 km deep. The model also predicts that the upwelling plumes cool mostly by lateral advection of heat by seepage parallel to the stratification, along fine-sand layers deposited by density currents and siliceous oozes. This circulation pattern is consistent with basaltic to ultramafic rocks interaction observed in the brine's geochemistry. At the same time, the slow motion of fluids in the basin sediments explain extensive fluid-sediment interaction in the Auka fluids (Paduan et al., 2018) that produced the deposition of significant amounts of base metal sulfides.

Model scaling relationships and observations elsewhere indicate that only faults <3 km in length appear to develop the conditions required to sustain the temperature gradients observed in the sediment-hosted Auka vent field. This could explain why other longer neighboring faults do not show signs of hydrothermal activity. Moreover, the relative transmissivity of the fault's damage zone is the strongest control on the width of the captured plume, and therefore on the heat flow decay length.

Acknowledgments
This is CICESE's Tectonophysics and Heat Flow Lab contribution No. 3. R. Negrete-Aranda and J. Contreras are grateful for the valuable comments to early versions of the ms. by Kuiper-Apfel. The authors thank A. Fisher for the use of his heat flow probe, the officers and crew of the *R/V Falkor*, *ROV SuBastian* pilots, the science participants of cruise FK181031, chief scientists R. Zierenberg, D. Caress, and V. Orphan as well as Sergio Arregui and Jose Mojarro for their technical support. R. N. Harris was supported by NSF OCE-1634536. J. Contreras acknowledges support from CICESE's internal project 644143. D. W. Caress and MBARI participants in FK181031 were supported by the David and Lucille Packard Foundation. The authors are also grateful to Jörg Hasenclever and Jean-Arthur Olive, who provided insightful comments on an earlier version of the manuscript.

Data Availability Statement

The heat flow data set used in this study can be accessed at: https://www.marine-geo.org/tools/search/Files.php?data_set_uid=29884.

References

Andersen, C., Rüpke, L., Hasenclever, J., Grevemeyer, I. & Petersen, S. (2015). Fault geometry and permeability contrast control vent temperatures at the Logatchev 1 hydrothermal field, Mid-Atlantic Ridge. *Geology*, *43*, 51–54. https://doi.org/10.1130/G36113.1

Balsamo, F., & Storti, F. (2010). Grain size and permeability evolution of soft-sediment extensional sub-seismic and seismic fault zones in high-porosity sediments from the Crotone basin, southern Apennines, Italy. *Marine and Petroleum Geology*, *27*, 822–837. https://doi.org/10.1016/j.marpetgeo.2009.10.016

Barron, J. A., & Bukry, D. (2007). Solar forcing of Gulf of California climate during the past 2000 yr suggested by diatoms and silicoflagellates. *Marine Micropaleontology*, *62*, 115–139. https://doi.org/10.1016/j.marmicro.2006.08.003

Barron, J. A., Bukry, D., & Dean, W. E. (2005). Paleoceanographic history of the Guaymas Basin, Gulf of California, during the past 15,000 years based on diatoms, silicoflagellates, and biogenic sediments. *Marine Micropaleontology*, *56*, 3–102. https://doi.org/10.1016/j.marmicro.2005.04.001

Becker, A., & Fisher, A. T. (1991). "A brief review of heat-flow studies in the Guaymas Basin, Gulf of California". In J. Paul Dauphin, & B. R. T. Simoneit (Ed.), *The gulf and peninsular province of the Californias*. American Association of Petroleum Geologists. https://doi.org/10.1306/M47542C33

Berndt, C., Hensen, C., Mortera-Gutierrez, C., Sarkar, S., Geilert, S., Schmidt, M., et al. (2016). Rifting under steam—How rift magmatism triggers methane venting from sedimentary basins. *Geology*, *44*, 767–770. https://doi.org/10.1130/G38049.1

Bialas, R. W., & Buck, W. R. (2009). How sediment promotes narrow rifting: Application to the Gulf of California. *Tectonics*, *28*. https://doi.org/10.1029/2008TC002394

Carslaw, H. S., & Jaeger, J. C. (1959). *Conduction of heat in solids* (2nd ed., pp. 978). Clarendon Press.

Clague, D. A., Caress, D. W., Dreyer, B. M., Lundsten, L., Paduan, J. B., Portner, R. A., et al. (2018). Geology of the Alarcon Rise, southern Gulf of California. *Geochemistry, Geophysics, Geosystems*, *19*, 807–837. https://doi.org/10.1002/2017GC007348

Cole, K., James, B., Haji-Sheikh, A., & Bahman, L. (2010). *Heat conduction using Greens functions* (Vol. 54, pp. 96–105). Taylor & Francis. https://doi.org/10.1016/j.marpetgeo.2014.02.019

Contreras, J., & Negrete-Aranda, R. (2014). A 1.5 D model of the steady-state thermal structure of detachment folds. *Marine and Petroleum Geology*, *54*, 96–105. https://doi.org/10.1016/j.marpetgeo.2014.02.019

Contreras-Pérez, J., Ramírez-Zerpa, N. & Negrete-Aranda, R. (2012). Modelos tectonoestratigráficos de las cuencas de Tiburón y Wagner en el norte del Golfo de California. *Revista mexicana de ciencias geológicas*, *29*(1), pp.140-157.

Crouch, S. L., Starfield, A. M., & Rizzo, F. J. (1983). Boundary element methods in solid mechanics. *ASME, Journal of Applied Mechanics*, *50*(3), 704–705. https://doi.org/10.1115/1.3167130

Cruse, A. M., Seewald, J. S., Saccocia, P. J., & Zierenberg, R. (2008). Hydrothermal fluid composition at Middle Valley, northern Juan de Fuca Ridge: Temporal and spatial variability. In R. P. Lowell, J. S. Seewald, A. Metaxas, & M. R. Perfit (Eds.), *Magma to Microbe: Modeling hydrothermal processes at ocean spreading centers, Geophysical Monograph Series*. American Geophysical Union. https://doi.org/10.1029/178GM08

Curewitz, D., & Karson, J. A. (1997). Structural settings of hydrothermal outflow: Fracture permeability maintained by fault propagation and interaction. *Journal of Volcanology and Geothermal Research*, *79*, 149–168. https://doi.org/10.1016/S0377-0273(97)00027-9

Davis, E. E., & Becker, K. (1994). Thermal and tectonic structure of Escanaba Trough; new heat-flow measurements and seismic-reflection profiles. In J. L. Morton, R. A. Zierenberg, & C. A. Reiss (Eds.), *Geologic, hydrothermal, and biologic studies at Escanaba Trough, Gorda Ridge, offshore Northern California*. (Vol. 2022, pp. 45–64). U.S. Geological Survey.

Davis, E. E., Chapman, D. S., Wang, K., Villinger, H., Fisher, A. T., Robinson, S. W., et al. (1999). Regional heat flow variations across the sedimented Juan de Fuca Ridge eastern flank: Constraints on lithospheric cooling and lateral hydrothermal heat transport. *Journal of Geophysical Research*, *104*, 17675–17688. https://doi.org/10.1029/1999JB900124

Davis, E. E., Wang, K., He, J., Chapman, D. S., Villinger, H., & Rosenberger, A. (1997). An unequivocal case for high Nusselt number hydrothermal convection in sediment-buried igneous oceanic crust. *Earth and Planetary Science Letters*, *146*, 137–150. https://doi.org/10.1016/S0012-821X(96)00212-9

DeMets, C., Gordon, R. G., & Argus, D. F. (2010). Geologically current plate motions. *Geophysical Journal International*, *181*(1), 1–80. https://doi.org/10.1111/j.1365-246x.2009.04491.x

Denlinger, R. P., & Holmes, M. L. (1994). A thermal and mechanical model for sediment hills and associated sulfide deposits along Escanaba Trough. In J. L. Morton, R. A. Zierenberg, & C. A. Reiss (Eds.), *Geologic, hydrothermal, and biologic studies at Escanaba Trough, Gorda Ridge, offshore Northern California*. (pp. 45–64). U.S. Geological Survey.

Escorza-Reyes, M., Perez-Cruz, L. L. & Fucugauchi, J. U. (2013). Paleoclimatic record of the last 18 ka cal BP in marine sediments from Pescadero Basin, southern Gulf of California. In *AGU Spring Meeting Abstracts* (Vol. 2013, pp. PP41B-02).

Farahat, N. X., Archer, D., & Abbot, D. S. (2017). Validation of the BASALT model for simulating off-axis hydrothermal circulation in oceanic crust. *Journal of Geophysical Research: Solid Earth*, *122*(8), 5871–5889. https://doi.org/10.1002/2016JB013758

Fisher, A. T., & Becker, K. (1991). Heat flow, hydrothermal circulation and basalt intrusions in the Guaymas Basin, Gulf of California. *Earth and Planetary Science Letters*, *103*, 84–99. https://doi.org/10.1016/0012-821x(91)90152-8

Fisher, A. T., Davis, E. E., & Becker, K. (2008). Borehole-to-borehole hydrologic response across 2.4 km in the upper oceanic crust: Implications for crustal-scale properties. *Journal of Geophysical Research: Solid Earth*, *113*. https://doi.org/10.1029/2007JB005447

Fisher, A. T., & Geoffrey Wheat, C. (2010). Seamounts as conduits for massive fluid, heat, and solute fluxes on ridge flanks. *Oceanography*, *23*, 74–87. https://doi.org/10.5670/oceanog.2010.63

Flores-Trujillo, J. G., Helenes, J., Herguera, J. C., & Orellana-Cepeda, E. (2009). Palynological record (1483–1994) of Gymnodinium catenatum in Pescadero Basin, southern Gulf of California, Mexico. *Marine Micropaleontology*, *73*, 80–89. https://doi.org/10.1016/j.marmicro.2009.06.009

Hannington, M. D., de Ronde, C. E. J., & Petersen, S. (2005). Seafloor tectonics and submarine hydrothermal systems. *Economic Geology*, *100*, 111–141. https://doi.org/10.5382/av100.06

Landau, L. D., & Lifshitz, E. M. (1987). *Fluid Mechanics, Course of theoretical physics* (2nd ed., Vol. 6). Butterworth-Heinemann. https://doi.org/10.1016/C2013-0-03799-1

León Robles, J. A. (2017). *Uso de redes de Boltzmann para la modelación de ujo a través de areniscas saturadas de agua. Tesis de maestría en Ciencias*. Centro de Investigación Científica y de Educación Superior de Ensenada.

Lister, C. R. B. (1972). On the thermal balance of a mid-ocean ridge. *Geophysical Journal International*, *26*, 515–535. https://doi.org/10.1111/j.1365-246X.1972.tb05766

Lizarralde, D., Axen, G. J., Brown, H. E., Fletcher, J. M., González-Fernández, A., Harding, A. J., et al. (2007). Variation in styles of rifting in the Gulf of California. *Nature*, *448*(7152), 466–469. https://doi.org/10.1038/nature06035

Lonsdale, P. (1995). Segmentation and disruption of the East Pacific Rise in the mouth of the Gulf of California. *Marine Geophysical Researches*, *17*, 323–359. https://doi.org/10.1007/BF01227039

Lonsdale, P., & Becker, K. (1985). Hydrothermal plumes, hot springs, and conductive heat flow in the Southern Trough of Guaymas Basin. *Earth and Planetary Science Letters*, *73*, 211–225. https://doi.org/10.1016/0012-821X(85)90070-6

Lonsdale, P., & Lawver, L. A. (1980). Immature plate boundary zones studied with a submersible in the Gulf of California. *The Geological Society of America Bulletin*, *91*, 555–569. https://doi.org/10.1130/0016-7606(1980)91<555:ipbzsw>2.0.co;2

Lowell, R. P. (2017). A fault-driven circulation model for the Lost City hydrothermal field. *Geophysical Research Letters*, *44*, 2703–2709. https://doi.org/10.1002/2016GL072326

Lowell, R. P., & Germanovich, L. N. (2004). Hydrothermal processes at mid-ocean ridges: Results from scale analysis and single-pass models. In C. R. German, J. Lin, & L. M. Parson (Eds.), *Mid-Ocean Ridges: Hydrothermal Interactions between the lithosphere and oceans, Geophysical Monograph Series* (Vol. 148, pp. 219–244). AGU.

Lowell, R. P., Rona, P. A., & Von Herzen, R. P. (1995). Seafloor hydrothermal systems. *Journal of Geophysical Research*, *100*, 327–352. https://doi.org/10.1029/94JB02222

Macias-Iñiguez, I., Yarbuh, I., Spelz-Madero, R., González-Fernández, A., Fletcher, J. M., Contreras, J., et al. (2019). Modo de extensión de la corteza y formación del Sistema Extensional de Cerralvo, sur del Golfo de California, a partir de datos de reflexión sísmica en 2D. *Revista Mexicana de Ciencias Geológicas*, *36*, 334–347. https://doi.org/10.22201/cgeo.20072902e.2019.3.1352

Martín-Barajas, A., González-Escobar, M., Fletcher, J. M., Pacheco, M., Oskin, M., & Dorsey, R. (2013). Thick deltaic sedimentation and detachment faulting delay the onset of continental rupture in the Northern Gulf of California: Analysis of seismic reflection profiles. *Tectonics*, *32*(5), 1294–1311. https://doi.org/10.1002/tect.20063

Monecke, R., Petersen, S., Hannington, M. D., Grant, H., & Samson, I. (2016). The minor endowment of modern seafloor massive sulfides and comparison with deposits hosted in ancient volcanic successions. *Reviews in Economic Geology*, *18*, 245–306.

Morin, R., & Silva, A. J. (1984). The effects of high pressure and high temperature on some physical properties of ocean sediments. *Journal of Geophysical Research*, *89*, 511–526. https://doi.org/10.1029/JB089iB01p00511

Negrete-Aranda, R., Contreras, J., & Spelz, R. M. (2013). Viscous dissipation, slab melting, and post-subduction volcanism in south-central Baja California, Mexico. *Geosphere*, *9*, 1714–1728. https://doi.org/10.1130/GES00901.1

Neumann, F., Negrete-Aranda, R., Harris, R. N., Contreras, J., Sclater, J. G., & González-Fernández, A. (2017). Systematic heat flow measurements across the Wagner Basin, northern Gulf of California. *Earth and Planetary Science Letters*, *479*, 340–353. https://doi.org/10.1016/j.epsl.2017.09.037

Olive, J. A., & Crone, T. J. (2018). Smoke without fire: How long can thermal cracking sustain hydrothermal circulation in the absence of magmatic heat? *Journal of Geophysical Research: Solid Earth*, *123*, 4561–4581. https://doi.org/10.1029/2017JB14900

Ondréas, H., Scalabrin, C., Fouquet, Y., & Godfroy, A. (2018). Recent high-resolution mapping of Guaymas hydrothermal fields (Southern Through), Cartographie haute résolution des champs hydrothermaux de la ride sud du bassin de Guaymas. *Bulletin de la Société Géologique de France*, *189*, 6. https://doi.org/10.1051/bsgf/2018005

Paduan, J. B., Zierenberg, R. A., Clague, D. A., Spelz, R. M., Caress, D. W., Troni, G., et al. (2018). Discovery of hydrothermal vent fields on Alarcón Rise and in Southern Pescadero Basin, Gulf of California. *Geochemistry, Geophysics, Geosystems*, *19*, 4788–4819. https://doi.org/10.1029/2018gc007771

Parsons, B., & Sclater, J. G. (1977). An analysis of the variation of ocean floor bathymetry and heat flow with age. *Journal of Geophysical Research*, *82*, 803–827. https://doi.org/10.1029/JB082i005p00803

Persaud, P., Tan, E., Contreras, J., & Lavier, L. (2017). A bottom-driven mechanism for distributed faulting in the Gulf of California rift. *Tectonophysics*, *719–720*, 51–65. https://doi.org/10.1016/j.tecto.2016.11.024

Peter, J. M., & Shanks, W. C. I (1992). Sulfur, carbon, and oxygen isotope variations in submarine hydrothermal deposits of Guaymas Basin, Gulf of California, USA. *Geochimica et Cosmochimica Acta*, *56*, 2025–2040. https://doi.org/10.1016/0016-7037(92)90327-F

Plattner, C., Malservisi, R., Dixon, T. H., Lafemina, P., Sella, G. F., Fletcher, J., & Suarez-Vidal, F. (2007). New constraints on relative motion between the Pacific Plate and Baja California microplate (Mexico) from GPS measurements. *Geophysical Journal International*, *170*, 1373–1380. https://doi.org/10.1111/j.1365-246X.2007.03494.x

Prol-Ledesma, R. M., Torres-Vera, M. A., Rodolfo-Metalpa, R., Angeles, C., Deveze, C. H. L., Villanueva-Estrada, R. E., et al. (2013). High heat flow and ocean acidification at a nascent rift in the northern Gulf of California. *Nature Communications*, *4*, 1–7. https://doi.org/10.1038/ncomms2390

Sleep, N. H., & Wolery, T. J. (1978). Egress of hot water from midocean ridge hydrothermal systems: Some thermal constraints. *Journal of Geophysical Research*, *83*, 5913–5922. https://doi.org/10.1029/JB083iB12p05913

Spelz, R. M., Lupton, J. E., Evans, L. J., Zierenberg, R. A., Clague, D. A., Neumann, F., & Paduan, J. B. (2015). Noble gas geochemistry of the newly discovered hydrothermal fields in the Gulf of California: Preliminary He-isotope ratios from the Alarcon Rise and Pescadero Basin vent sites. In *AGU Fall Meeting Abstracts*. Retrieved from https://ui.adsabs.harvard.edu/abs/2015AGUFMOS23C2028S/abstract

Spinelli, G. A., Giambalvo, E. R., & Fisher, A. T. (2004). Sediment permeability, distribution, and influence on fluxes in oceanic basement. In E. E. Davis, & H. Elderfield (Ed.), *Hydrogeology of the oceanic lithosphere*. Cambridge University Press.

Torabi, A., & Berg, S. S. (2011). Scaling of fault attributes: A review. *Marine and Petroleum Geology*, *28*, 1444–1460. https://doi.org/10.1016/j.marpetgeo.2011.04.003

Von Damm, K. L. (1990). Seafloor hydrothermal activity: Black smoker chemistry and chimneys. *Annual Review of Earth and Planetary Sciences*, *18*(1), 173–204. https://doi.org/10.1146/annurev.ea.18.050190.001133

Von Damm, K. L., Bischoff, J. L., & Rosenbauer, R. J. (1991). Quartz solubility in hydrothermal seawater; an experimental study and equation describing quartz solubility for up to 0.5 M NaCl solutions. *American Journal of Science*, *291*, 977–1007. https://doi.org/10.2475/ajs.291.10.977

Wagner, W. & Kretzschmar, H. J. (2007). *International steam tables-properties of water and steam based on the industrial formulation IAPWS-IF97*. Springer Science & Business Media. https://doi.org/10.1007/978-3-662-53219-5

Williams, D. L., Becker, K., Lawver, L. A., & Von Herzen, R. P. (1979). Heat flow at the spreading centers of the Guaymas Basin, Gulf of California. *Journal of Geophysical Research*, *84*, 6757–6769. https://doi.org/10.1029/JB084iB12p06757

Wolery, T. J., & Sleep, N. H. (1976). Hydrothermal circulation and geochemical flux at mid-ocean ridges. *The Journal of Geology*, *84*, 249–275. https://doi.org/10.1086/628195

Zierenberg, R. A., Fouquet, Y., Miller, D. J., Bahr, J. M., Baker, P. A., Bjerkgård, T., et al. (1998). The deep structure of a seafloor hydrothermal deposit. *Nature*, *392*, 485–488. https://doi.org/10.1038/33126

Zierenberg, R. A., Koski, R. A., Morton, J. L. & Bouse, R. M. (1993). Genesis of massive sulfide deposits on a sediment-covered spreading center, Escanaba Trough, southern Gorda Ridge. *Economic Geology*, *88*, 2069–2098. https://doi.org/10.2113/gsecongeo.88.8.2069

Zierenberg, R. A., & Miller, D. J. (2000). Overview of Ocean Drilling Program Leg 169: Sedimented ridges II. In R. A. Zierenberg, Y. Fouquet, D. J. Miller, & W. R. Normark (Eds.), *Proceeding of ODP Scientific results* (pp. 1–39). Ocean Drilling Program. https://doi.org/10.2973/odp.proc.sr.169.119.2000